Research Paper

Design and optimization of thermoelectric generators for harnessing geothermal anomalies: A computational model and validation with experimental field results

Patricia Alegría *, Leyre Catalán, Miguel Araiz, Irantzu Erro, David Astrain

Institute of Smart Cities, Public University of Navarre, Pamplona, Spain

ARTICLE INFO

ABSTRACT

Thermoelectric generators have been recently proved to be a feasible alternative to harness hot dry rock fields with very promising results transforming the geothermal heat into electricity. This research deepens in the study of these generators, developing a versatile computational model that serves as a tool to design and optimize this type of thermoelectric generators. This tool is important to develop this thermoelectric technology on a large scale, to produce clean and renewable electrical energy especially in the Timanfaya National Park, in Lanzarote (Spain), where some of the most important shallow geothermal anomalies in the world are located, in order to promote self-consumption in this zone. However, it could be employed in other areas with different boundary conditions. The model, based in the finite difference method applied to the thermal-electrical analogy of a geothermal thermoelectric generator, has been validated with the experimental field results of two thermoelectric generators installed in two different zones of geothermal anomalies. It has achieved a relative error of less than 10% when predicting the power and between 0.5–1.6% in the annual energy generation, what makes it a very reliable and useful computational tool. The developed model has been employed for the first time to estimate the electrical energy that could be generated if harnessing the characterized area of anomalies in Lanzarote. Here, given the continuity of geothermal energy, 7.24 GWh per year could be generated, which means annually 1.03 MWh/m^2.

1. Introduction

Every effort is needed to empower the use of renewable energy sources, especially in zones with more need for clean energy like the Canary Islands (Spain), which have an isolated electric system and a 98% dependence on fossil fuels for their primary energy [1,2]. As a matter of fact, the European Commission signed in 2017 the policy statement on Clean Energy for the Islands of the European Union (EU), recognizing their potential to be the architects of their own energy transition, as well as the opportunity to use these territories as a testing ground for energy transition technologies or policies that can afterwards be exported to the mainland [3]. In this regard, one objective of the Sustainable Energy Strategy in the Canary Islands, is to promote innovative energy projects, with new technologies that permit the use of high temperature geothermal energy for electricity generation [4].

The Canary Islands have a volcanic origin, which is notably present nowadays. For instance, the island of Lanzarote is one of the most important zones with geothermal anomalies in the world, which makes

it suitable for installing thermoelectric generators, that permit maintaining the high natural value of the island unspoilt. There are two large fractures that cross this island in the NNE-SSW and NE-SW directions [5]. The eruption that occurred between 1730 and 1736 in the area where the Timanfaya National Park is currently located, was one of the largest eruptions in history, and has given rise to numerous scientific studies to understand its origin and characteristics. A magnetotelluric study of the Timanfaya area evidenced the existence of a mass of highly conductive magma at an approximate depth of 4 km [6]. Diez et al. estimated the volume of this magmatic intrusion as a body with a radius of 200 ± 100 m characterized by a convective system in which heat energy is transmitted through deep fractures in the rock [7]. This magma body is responsible for the thermal anomalies that exist a few meters from the surface on this island. Due to the magma heating up the air inside the porous rocks, there are hot gases (98% Nitrogen) rising through the surface by means of density difference [8,9]. However, despite numerous studies, it has not been possible to fully characterize the surface of the island where these anomalies exist. Most of the known

---

* Corresponding author.
E-mail address: patricia.alegria@unavarra.es (P. Alegría).

Nomenclature

Variables

ΔP_{sat}	Difference in the saturation pressure corresponding to ΔT_{sat} (Pa)
ΔT_{sat}	Difference between the wall and the saturation temperatures (°C)
ΔT	Temperature difference (°C)
$\dot{Q}$	Heat flux (W)
ϵ	Ratio between the equivalent radius
η	Efficiency
γ	Surface tension (N/m)
λ_c	$\lambda_c = \pi + 1/(\sqrt{\pi} \cdot \epsilon)$
μ	Dynamic viscosity (Pa $\cdot$ s)
v	Kinematic Viscosity (m^2/s)
ψ	Dimensionless constriction resistance
τ	$\tau = e_c/\sqrt{A_c/\pi}$
A	Area (m^2)
Bi	Biot Number $Bi = h_b \cdot (\sqrt{A_c}/\pi)/k$
cp	Specific heat (J/kg $\cdot$ K)
D	Diameter (m)
e	Thickness (m)
G	Total mass flow per unit area
g	Gravity acceleration (m/s^2)
h	Heat transfer convection coefficient (W/m^2 $\cdot$ K)
i_{lg}	Latent heat of vaporization (J/kg)
J_g	Dimensionless vapor velocity
k	Thermal conductivity (W/m $\cdot$ K)
L_{ch-fin}	Characteristic length of a fin $L_{ch-fin} = L_{fin} + (e_{fin}/2)$
L_{ch}	Characteristic length (m)
M	Number of thermoelectric modules
m_{fin}	$m_{fin} = \sqrt{2 \cdot h_{conv}^H/k \cdot e_{fin}}$
N	Number
P	Electric power (W)
p_r	Reduced pressure
Pr	Prandtl Number $Pr = cp \cdot \mu/k$
R	Thermal resistance (K/W)
Re	Reynolds Number $Re = v \cdot L_{ch}/v$
T	Temperature (°C)
V	Velocity (m/s)
V	Voltage (V)
y	Mass fraction
Z	Shah correlation parameter: $Z = (1/x - 1^{0.8} p_r^{0.4})$
i	Node number i
j	Node number j

Subscripts and Superscripts

amb	Ambient
b	Boiling
C	Cold side
c	Condensation
co	Contact
const	Constriction
conv	Convective
eq	Equivalent
ev	Evaporator
ext	Exterior
g	Gas
geoth	Geothermal
H	Hot side
k	Conductive
l	Liquid
n	Semiconductor n
p	Semiconductor p
par	Parallel connection
real	Real
sat	Saturation
sat	Saturation
ser	Series connection
sf	Surface
sim	Simulated
sup	Per unit of area
tc	Termocouple
u	Joint material

Abbreviations

CHE	Cold side Heat Exchanger
EGS	Enhanced Geothermal System
EU	European Union
FDM	Finite Difference Method
GTEG	Geothermal Thermoelectric Generator
HDR	Hot Dry Rock Field
HHE	Hot side Heat Exchanger
HT	High Temperature
MT	Medium Temperature
PV	Photovoltaic
TEG	Thermoelectric Generator
TEM	Thermoelectric Module
TNP	Timanfaya National Park
TPCT	Two Phase Closed Thermosyphon

anomalies are located on three crater rims in three specific zones: *Islote Hilario*, over an area of 3000 m^2 with the highest temperatures reaching 610 °C at 13 m depth and around 500 in the surface; *Casa de los Camelleros*, over a 4000 m^2 area and with surface temperatures around 200 °C; and *Timanfaya Massif*, a complex system of craters with thermal anomalies that reach 250 °C [10]. All these anomalies were estimated to be over an area of 11 000 m^2 [11]. This zone is a Hot Dry Rock field (HDR), which until now could only be exploited by Enhanced Geothermal Systems (EGS), an invasive geothermal technology that requires fracturing the rock to insert water. That is why, despite the existing geothermal potential, nowadays it is not being harnessed due to the difficulties implicit to the existing geothermal power plants: their high environmental impact added to the high initial investment and costs of water and maintenance.

Here, thermoelectric generators have been proved to be a feasible alternative [12]. Even though they reach lower efficiencies compared to conventional geothermal plants working with Rankine cycles, they have important advantages as the absence of moving parts, their compactness, and the low maintenance required. Thermoelectric generators are composed by thermoelectric modules, that are solid-state devices, capable of transforming a heat flow directly into electricity thank to the Seebeck effect [13]. These modules consist of soldered junctions, called thermocouples, of two types of semiconductors; a p-type semiconductor and an n-type semiconductor of similar Seebeck coefficient, thermal conductivity, and electrical resistivity, whose hot and cold junctions are

at different temperatures. Thermocouples that absorb heat are located on one side of the module (called hot side), and those that release heat on the opposite side (called cold side). In addition, the modules contain a plate of ceramic material on each side to provide rigidity. The output potential of a thermocouple made of semiconductor materials is relatively low. For this reason, a large number of these thermocouples are connected electrically in series and thermally in parallel.

In order to maximize power generation, as the efficiency of a thermoelectric module depends on the temperature difference between its sides, to improve this thermal difference, a thermoelectric generator requires heat exchangers, both in its cold and hot side. These heat exchangers must present the lowest possible thermal resistance, so that they are more efficient making the temperature in each side of the modules closer to that of the corresponding thermal reservoir. It has been demonstrated that a 10% reduction in the thermal resistance of the heat exchangers produces a 8% increase in the power generated [14]. Furthermore, to maximize the net power generation, it is very important to avoid moving parts by employing passive heat exchangers, that do not present auxiliary consumption.

Due to their low efficiency compared to other conventional technologies, few geothermal thermoelectric generators can be found in the literature, and most of them employ moving parts and auxiliary consumption, thus reducing the net power and requiring maintenance. For instance, Liu et al. developed two prototypes, estimating a total generation of 500 W and 1 kW respectively [15,16], without taking into account the consumption of the cold side heat exchanger, which required a pump to move a fluid. Suter et al. modelled a 1 kW thermoelectric generator using water entering at $140\,°C$ and leaving the system at $20\,°C$, but it was a computer study and their proposed system required moving parts to circulate the fluid [17]. Ahiska and Mamur developed a portable TEG for low geothermal temperatures, obtaining a maximum power output of 41.6 W (2.08 W per TEM) with a temperature difference between the TEM's sides of $67\,°C$ [18]. Dell et al. developed a thermoelectric generator to harness a geothermal steam pipe, managing to produce more than 5 W (0.83 W per module) with a $130\,°C$ temperature difference between reservoirs [19]. Another example is the test that Li et al. did at the Bottle Rock Geothermal Power Plant (California, USA), where they used steam from a geothermal well as a heat source, cooled by a water flow on the cold side, estimating that their geothermal thermoelectric device could generate 500 W (3.6 W per TEM), but requiring moving parts, and thus, extra consumption, to circulate the cooling fluid. More recently, Zhao developed a geothermal thermoelectric generator with a passive heat exchanger on the hot side and cooled with a pumping system on the cold side [20], achieving a maximum output power of 10.85 W, but again, without taking into account the auxiliary consumption of the pumping system.

The development of geothermal thermoelectric generators without moving parts is very important in order not to lose the main advantages of thermoelectricity: robustness, lack of maintenance nor auxiliary consumption, and is very recent. The first passive GTEG was proposed by Catalán et al. [21], who obtained a 54% efficiency improvement with respect to a finned dissipator by means of biphasic thermoyphons as cold side heat exchangers, and developed a prototype of 3.2 W net output per module with no moving parts. Alegría et al. [12] characterized in laboratory a GTEG for medium temperature geothermal anomalies (MT) without moving parts, and were able to install it in Timanfaya National Park, demonstrating the feasibility of the technology for the first time in real conditions, working for more than 2 years in perfect operation without the need for maintenance and generating between 2.09 and 2.78 W per module [22]. Thank to this development, they could finally install a thermoelectric generator in the area with the highest temperature (HT) geothermal anomalies recorded in Lanzarote, reaching a generation of 4.5 W per module, 36 W total, working also without maintenance and generating more than 280 kWh of energy per year [23]. These include thermosyphons as heat exchangers, which

makes them totally passive, with no auxiliary consumption, and are the only geothermal thermoelectric generators installed an operating in a real geothermal field.

Once demonstrated the viability, the design of a larger-scale installation is needed in order to take advantage of the geothermal anomalies in the island of Lanzarote, which are currently untapped. Here, the development of a computational tool that permits designing such an installation depending on the conditions of the environment is of great importance. For that reason, the aim of this work is to develop a computational model capable of simulating the behaviour of these novel thermoelectric generators depending on different parameters as the ambient conditions (temperature and wind) and geothermal temperatures.

Due to the complexity of heat transmission, electric and thermoelectric phenomena in a thermoelectric generator, different computational models have been developed along the years to solve the corresponding equations and have become indispensable tools for designing and optimizing generators in real applications, thus reducing costs in the required prototypes and experiments. The first one was the model to simulate the behaviour of one thermoelectric module [24] from which other numerical methods were developed including heat exchangers on both sides of the module [25,26]. Astrain et al. were the precursors of the application of the finite differences method to develop a computational model capable of completely solving any type of thermoelectric system with very favourable results in cooling, including heat exchangers and thermal reservoirs, and also considering the influence of temperature on thermoelectric phenomena, as well as the effects of insulating materials and junctions between semiconductors [27]. Then, Martinez et al. developed a simulation model of thermoelectric generators, which predicts the behaviour of a complete generator, including heat exchangers, heat source and sink, without neglecting any thermoelectric effect (Seebeck, Peltier and Thomson effects), and considering the influence of temperature and contact, both thermal and electrical. They were able to simulate the steady state and the transient, accurately, quickly and reliably, with relative errors lower than 10% between real and simulated values of the output variables [28,29]. Aranguren et al. and Araiz et al. developed similar computational models to harness waste heat for thermoelectric generation, including determining factors such as the occupancy factor, the mass flow of the cooling fluids and the decrease in the temperature of the gases [30], thus, Araiz et al. obtained deviations of less than $\pm 9\%$ [31]. Regarding geothermal energy, Catalán et al. developed a model also based on the finite difference method, being able to simulate the behaviour of geothermal thermoelectric generators of different characteristics with a relative error of less than 8%, and partially validated it with experimental results obtained in laboratory [32,33].

In the present work, a computational model is developed and includes for the first time a validation with field experimental results to simulate the behaviour of thermoelectric generators to harness hot dry rock fields. The results of the two geothermal thermoelectric generators currently operating in the HDR field in the Timanfaya National Park are employed for the experimental validation. As mentioned, the final objective is to obtain a powerful tool to develop and optimize future installations, thus reducing time and costs of experimentation. Therefore, as an example of the capability of the developed model, it has been used to calculate the potential of electrical energy generation from the geothermal anomalies in Lanzarote, by designing a large-scale installation depending on the environmental and geothermal conditions.

Hence, although the geothermal thermoelectric generators taken as reference were analysed in the aforementioned studies [22,23], for a better understanding of this work, the GTEGs are deeply described in Section 2. Then, Section 3 details the developed computational model, which is subsequently validated by means of the experimental results. Afterwards, Section 4 employs the developed model to calculate the potential to generate electricity in Lanzarote, and finally, Section 5 contains the conclusions of this research work.
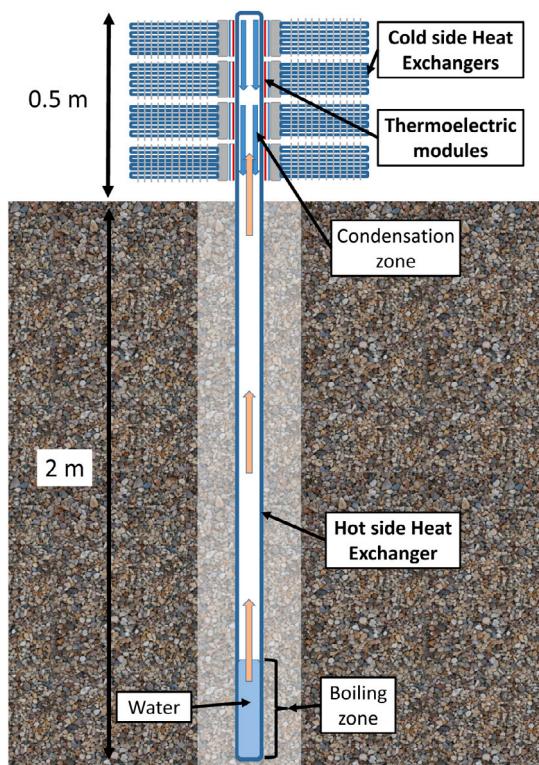
Fig. 1. Schematic of the geothermal thermoelectric generators installed in field.

Fig. 2. Geothermal thermoelectric generator for medium temperature geothermal anomalies installed in *Casa de los Camelleros*, Timanfaya National Park [22].

2. Description of the geothermal thermoelectric generators installed in field

To develop a computational model that reproduces the operation of a geothermal thermoelectric generator, it is important to know deeply how it works.

As mentioned, only two GTEGs are operating in field, both in Timanfaya National Park, in the island of Lanzarote, Spain. Each of these GTEGs, represented in Fig. 1, can be divided in three parts: the hot side heat exchanger (HHE), the thermoelectric modules (TEMs), and the cold side heat exchangers (CHEs). Both heat exchangers are completely passive and work by means of phase change. The HHE is a two phase closed thermosyphon (TPCT), which is partially inserted in a borehole. As the water inside absorbs the geothermal heat, it boils, rising until the upper part of the thermosyphon, which is over the ground. Here, the vapour condenses, releasing the latent heat to the thermoelectric modules, that are located outside the surface. These TEMs directly transform part of the received heat into electricity, and the rest of the heat must be dissipated into the ambient by the CHE that each module has in its cold side. These CHEs consist of a plate base with 4 heat pipes with water inside, working also by phase change, and have aluminium fins in order to increase the convection area and improve heat transmission to the environment. As the figure shows, the TEMs are distributed in different levels, with two TEMs in each level.

The first generator (MT-GTEG), shown in Fig. 2, was installed in August 2020 in the area of *Casa de los Camelleros*, in a borehole with emerging hot gases with a similar composition to that of the air [9], at a temperature of around 170 °C [22]. Here, the TPCT is made of copper and includes fins outside the boiling zone in order to improve heat transmission by conduction and convection, respectively. It includes 16 thermoelectric modules (Marlow TG-12-8-LS [34]) divided in two thermosyphons; one with 10 TEMs, with an average efficiency of 3.26%, generating a maximum power of 2.09 W per module with a temperature difference between sources of 158 °C, and another with 6 TEMs, an average efficiency of 3.57%, generating a maximum of 2.78 W per module. This study demonstrated the feasibility of this technology to harness geothermal anomalies, as well as the reduction in the efficiency with the increase of thermoelectric modules in one thermosyphon. This effect, demonstrated first computationally in [32] and then experimentally in [12], is due to the fact that each module has its own CHE, but they all share one HHE. For this reason, as the number of thermoelectric modules increases, the heat absorbed from the borehole is greater, which decreases the temperature on the hot side of the TEMs, and thus decreases their efficiency. This effect was also demonstrated in laboratory for the HT-GTEG in [23].

In order to evacuate the gases from the borehole, a deflector was installed. The GTEG is oriented to the predominant wind direction (N-NE), so that the wind directs the hot gases towards the other direction (S-SW).

The second GTEG (HT-GTEG), installed in June 2021 in the zone with the highest temperatures, *Islote Hilario*, is operating in a borehole with gases emerging at 465 °C, and it contains the same type of heat exchangers but only 8 thermoelectric modules in one only thermosyphon, as can be seen in Fig. 3 [23]. Moreover, the thermosyphon is made of steel due to its poper mechanical properties at such high temperature and does not include fins. This GTEG has achieved a maximum generation of 4.5 W per module, with a temperature difference between reservoirs of 444 °C and presents an efficiency in average conditions of 4.28%.

As Fig. 4 shows, the energy generation is more stable than the previous one, with an average deviation with respect to the mean value of daily energy generated of 2.05% in the MT-GTEG and 0.97% in the HT-GTEG, thanks to the improvement in the deflector, which in this case release the hot gases even further from the cold side heat exchangers, permitting not to decrease its efficiency those days where the wind direction is S-SW, opposite to the predominant.

As mentioned, in this work, a computational model able to simulate the energy generated is developed, using the available data of field operation to validate it, and employed afterwards to design new thermoelectric generators to harness geothermal anomalies depending on the environment conditions. Thus, regarding again the diagram of the GTEG in Fig. 1, the computational model must consider each part of the generator: the hot side heat exchanger, the thermoelectric modules, the cold side heat exchangers, the union between these pieces, as well as every phenomena that takes place in each mentioned part.

3. Development of the computational model

3.1. Model description

The model is based in the finite difference method (FDM), which is an approximate method for solving partial differential equations.

i. all materials are homogeneous, with uniform composition and structure

ii. the insulation of the electric circuit is perfect and the electric current is one-dimensional

iii. the heat flow is also one-dimensional, so lateral heat losses are neglected

iv. only steady state is considered

v. there is no subcooling or superheating in the heat exchangers

The thermal resistances of each part of the generator have been modelled dividing the generator in three parts, the hot side heat exchanger (R^H), the thermoelectric modules (R^{TEM}), and the cold side heat exchangers (R^C). These thermal resistances are detailed respectively in Sections 3.1.1–3.1.3.

Then, to join the three parts together, it is necessary to consider the thermal contacts due to the tiny air gaps that remain between the surface when two parts are assembled as a consequence of their roughness. In the GTEGs considered here, graphite sheets have been added between the surfaces in the hot and the cold sides of the modules in order to reduce these thermal contact resistances (R_{co}^H and R_{co}^C) [12,22,23]. Their value depend on the roughness of the materials and the pressure distribution in the assembly process.

The thermal-electrical analogy of the generator has been represented in Fig. 5, showing the simple thermal resistance schematic in Fig. 5(a), and the extended in Fig. 5(b), where the thermal resistances of each part of the generator, which are explained in the following subsections, have been represented.

Finally, applying the implicit finite difference method to the heat conduction equation, the numerical resolution is carried out in each node i by an iterative method with Eq. (1), considering a permanent regime and being j each adjacent node, until obtaining a tolerance between the new and the last temperatures calculated lower than 0.01.

$$\sum_j \frac{T_j - T_i}{R_{ij}} + \dot{Q}_i = 0 \tag{1}$$

3.1.1. Hot side heat exchanger

The hot side heat exchanger (HHE) consists of a two-phase closed thermosyphon which contains water as working fluid. It is responsible for absorbing heat from the air in the borehole by convection, and transport it to the hot side of the thermoelectric modules by means of phase change of the water inside.

The HHE has a total thermal resistance R_{total}^H that corresponds to Eq. (2), which is the sum of the convection thermal resistance (R_{conv}^H, Eq. (3)), the conduction in the evaporation zone (R_{k1}^H, Eq. (6)), the boiling and condensation resistances (R_b^H and R_c^H), whose coefficients are calculated according to Forster [36] and Rohsenow [37], respectively, and finally, the last thermal resistance in the condensation zone (R_{k2}^H, Eq. (15)), which is composed of a conduction resistance ($R_{k2,cond}^H$, Eq. (11)) and a constriction resistance ($R_{k2,const}^H$, Eq. (12)) because condensation occurs in an area bigger than that of the module.

$$R_{total}^H = R_{conv}^H + R_{k1}^H + R_b^H + R_c^H + R_{k2}^H \tag{2}$$

The first thermal resistance represents the convection between the gases and the TPCT inside the borehole, and contemplates whether fins are included to improve heat transfer or not. It is expressed in Eq. (3), where h_{conv}^H is the convection coefficient obtained from the Nusselt expression of Sieder y Tate for forced convection inside tubes (Eq. (4)) [38], A_{conv}^H is the area of TPCT in contact with the hot gases (taking into account the fins, in case they exist, and the height of the water inside the thermosyphon), and η_{fins} is the fins efficiency, calculated by means of Eq. (5) [39].

$$R_{conv}^H = \frac{1}{h_{conv}^H \cdot A_{conv}^H \cdot \eta_{fins}^H} \tag{3}$$

Fig. 3. Geothermal thermoelectric generator for high temperature geothermal anomalies installed in *Islote Hilario*, Timanfaya National Park [23].
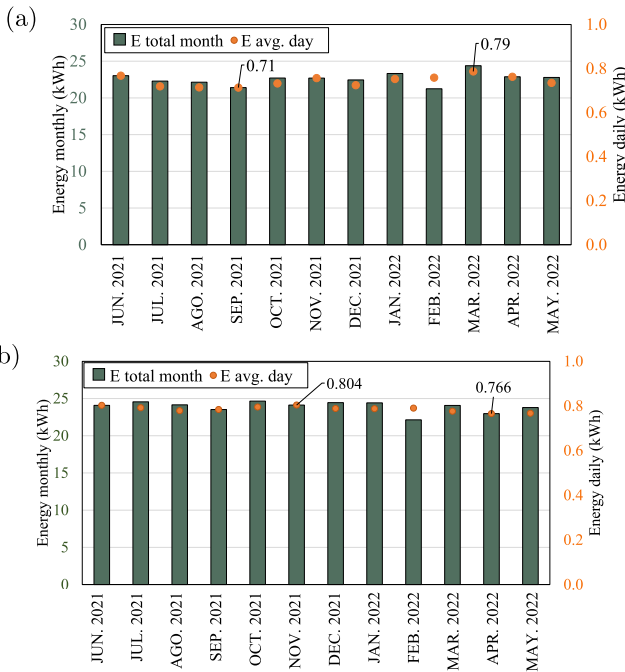

Fig. 4. Energy generated per month and per day during 2021–2022. (a) By the MT-GTEG. (b) By the HT-GTEG.

The aim of FDM is to replace a continuous field problem with infinite degrees of freedom by a discrete field with a finite number of nodes. The partial derivatives of the unknown function are approximated by the difference quotients at a set of finite discretization points, then, the original partial differential equation is transformed into a set of algebraic equations. The solution of these simultaneous equations is the approximate solution of the original problem [35].

This model takes as a reference the one previously developed by Catalán et al. for geothermal thermoelectric generators [32], which follows the electrical analogy between heat transfer and electricity, and considers for the first time heat exchangers based on the phase change on both sides of thermoelectric modules. The thermal-electrical analogy is derived from the application of the finite difference method to the heat conduction equation, thus discretizing the system that simulates the generator into several nodes.

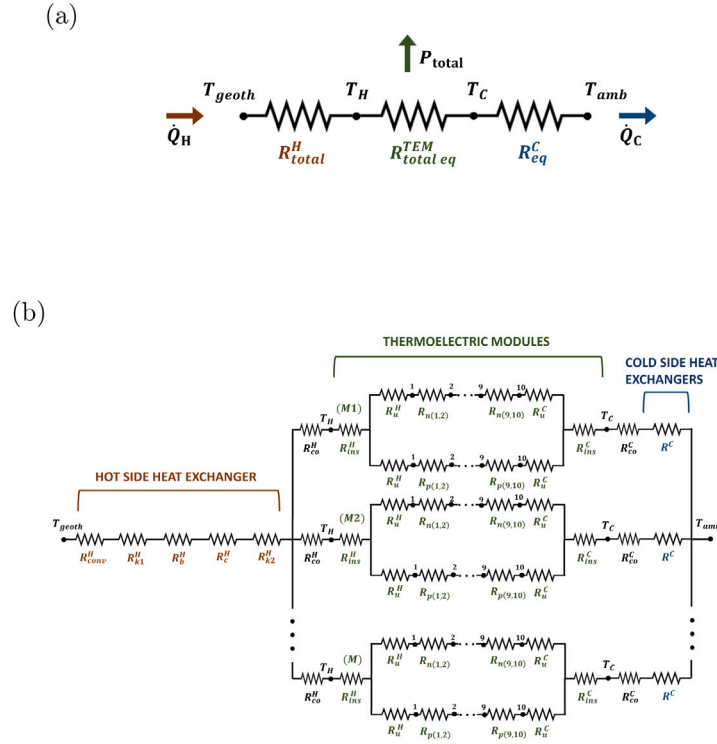The following hypothesis are considered for the modelling:

(a)

(b)

Fig. 5. Thermal-electrical analogy of the system. (a) Reduced. (b) Extended.

$$Nu = 0.027 \cdot Re^{0.8} \cdot Pr^{1/3} \cdot \left(\frac{\mu}{\mu_{sf}}\right)^{0.14} \tag{4}$$

$$\eta_{fin} = 1 - \frac{N_{fin} \cdot A_{fin}}{A_{conv}^H} \left(1 - \frac{\tanh(m_{fin} \cdot L_{ch-fin})}{m_{fin} \cdot L_{ch-fin}}\right) \tag{5}$$

Then, R_{k1}^H represents the conduction resistance of the wall of the thermosyphon in the evaporation zone, which is considered the area occupied by the water inside. As it is a cylindrical TPCT, this thermal resistance is calculated by means of Eq. (6) [38].

$$R_{k1}^H = \frac{\ln\left(D_{ext}^H/D_{int}^H\right)}{2 \cdot \pi \cdot L \cdot k^H} \tag{6}$$

The heat transmitted through the wall of the TPCT is responsible for the evaporation of part of the fluid, thus, this is simulated thanks to the boiling thermal resistance R_b^H, for which the boiling coefficient is necessary (Equation (7)). Assuming that nuclear boiling takes place, that is to say, vapor bubbles are formed in the heat transfer surface and then are released and transported to the main flow, the expression proposed by Forster and Zuber in 1955 is employed (Eq. (8)) [36].

$$R_b^H = \frac{1}{h_b^H \cdot A_b^H} \tag{7}$$

$$h_b^H = \frac{0.00122 \cdot \Delta T_{sat}^{0.24} \cdot \Delta P_{sat}^{0.75} \cdot cp_l^{0.45} \cdot d_l^{0.49} \cdot k_l^{0.79}}{\gamma^{0.5} \cdot i_{lg}^{0.24} \cdot \mu_l^{0.29} \cdot d_g^{0.24}} \tag{8}$$

The vapour ascends then due to density difference until the upper part, where the thermoelectric modules are located, and condenses. To calculate the condensation thermal resistance, it is necessary to consider the condensation area of all the TEMs and the condensation coefficient (Eq. (9)). The phenomena considered is film condensation in a vertical tube, that is why the expression for a vertical plate is extended both for the interior and the exterior surfaces, when the diameter is high compared to the film thickness. The heat transmission coefficient is determined by Eq. (10) [37], which neglects the effects of film convection and assumes a constant wall temperature, given that

condensation occurs at a constant saturation temperature.

$$R_c^H = \frac{1}{h_c^H \cdot A_c^H} \tag{9}$$

$$h_c^H = 0.943 \cdot \left[\frac{k_l^3 \cdot d_l \cdot (d_l - d_g) \cdot g \cdot i_{lg}}{\mu_l \cdot \Delta T_{sat} \cdot L_{ch}}\right]^{\frac{1}{4}} \tag{10}$$

Finally, the thermal resistance R_{k2}^H represents, on the one hand the conduction taking place in the condensation zone. In this case, given that the TEMs are in contact with the upper part of the thermosyphon, the heat conduction expression in plate surfaces was considered (Eq. (11)) [38]. Here, subindex c is referred to the condensation part of the thermosyphon.

$$R_{k2,cond}^H = \frac{e_c^H}{k^H \cdot A_c^H} \tag{11}$$

On the other hand, given that condensation occurs in a bigger area than the modules area, the effect of constriction appears, causing an increase in the thermal resistance. In this model, the expression estimated by Lee et al. [40] was consider.

$$R_{k2,const}^H = \frac{\Psi^H}{N_{TEM} \cdot k^H \cdot \sqrt{A_{TEM}}} \tag{12}$$

where N_{TEM} represents the number of thermoelectric modules, k^H is the thermal conductivity of the material, A_{TEM} is the area of a thermoelectric module and Ψ^H is the dimensionless constriction resistance which follows Eq. (13), where ϵ^H is the ratio between the equivalent radius of a module and the one of the region where condensation occurs. Φ_c^H follows Eq. (14).

$$\Psi^H = \frac{1}{2} \cdot (1 - \epsilon^H)^{3/2} \cdot \Phi_c^H \tag{13}$$

$$\Phi_c^H = \frac{\tanh(\lambda_c^H \cdot \tau^H) + \frac{\lambda_c^H}{Bi^H}}{1 + \frac{\lambda_c^H}{Bi^H} \cdot \tanh(\lambda_c^H \cdot \tau^H)} \tag{14}$$

Then, the thermal resistance R_{k2}^H is calculated by means of the sum of the conduction and constriction resistances:

$$R_{k2}^H = R_{k2,cond}^H + R_{k2,const}^H \tag{15}$$

3.1.2. Thermoelectric modules

The following thermal resistances correspond to the thermoelectric modules. These are composed of different thermocouples connected electrically in series and thermally in parallel. Each thermocouple is composed of an n-type semiconductor connected through a conductive material to a p-type semiconductor.

To model all phenomena occurring simultaneously in a thermoelectric module, in each thermocouple, the semiconductors are discretized into 10 nodes, since this leads to accurate results without increasing the computational cost [30,41,42], and allows considering a temperature-dependent properties.

Since the dominant heat transfer mechanism is conduction, all the thermal resistances of the n and p semiconductors are calculated by Eqs. (16) and (17) respectively, in which N_{tc} thermocouples composing a thermoelectric module have been considered to be thermally connected in parallel, similarly to the N_{TEM} thermoelectric modules.

$$R_{n(i,i+1)} = \frac{L_n/9}{N_{TEM} \cdot N_{tc} \cdot k_{n(i,i+1)} \cdot A_n} \quad i = 1-9 \tag{16}$$

$$R_{p(i,i+1)} = \frac{L_p/9}{N_{TEM} \cdot N_{tc} \cdot k_{p(i,i+1)} \cdot A_p} \quad i = 1-9 \tag{17}$$

The semiconductor lengths are included in these equations as L_n and L_p. Their thermal conductivities are $k_{n(i,i+1)}$ and $k_{p(i,i+1)}$, calculated at the average temperature of their surrounding nodes i and $i+1$, and the areas of their cross sections are A_n y A_p.

This model also considers the thermal resistance of the junction material between semiconductors, although it is sometimes neglected due to the high conductivity of the junction material compared to that of semiconductors. As shown in Eq. (18), half of the material is considered in part n and the other half in part p.

$$R_u^H = R_u^C = \frac{L_u}{N_{TEM} \cdot N_{tc} \cdot k_u \cdot A_u/2} \tag{18}$$

The last thermal resistances considered in the TEMs are those corresponding to the electrical insulation material that protects the internal circuit and provides firmness to each module, shown in Eq. (19).

$$R_{ins}^H = R_{ins}^C = \frac{L_{ins}}{N_{TEM} \cdot k_{ins} \cdot A_{ins}} \tag{19}$$

Then, the total thermal resistance for a thermoelectric module (R_{total}^{TEM}) is composed by the summation of all the n-type semiconductors ($R_{n(i,i+1)}$) and the p-type semiconductors ($R_{p(i,i+1)}$) (summed in parallel), plus the unions (R_u^H and R_u^C) and the insulation in the hot and the cold side (R_{ins}^H and R_{ins}^C).

$$R_{total}^{TEM} = \left[\sum_{i=2}^{9} \left(R_{n(i,i+1)} \right) + \sum_{i=2}^{9} \left(R_{p(i,i+1)} \right) \right]_{II} + R_u^H + R_u^C + R_{ins}^H + R_{ins}^C \tag{20}$$

In addition to the thermal resistances of the TEMs, it is necessary to consider heat flows at the semiconductor nodes in order to simulate the thermoelectric effects that take place. Each node generates heat due to Joule and Thomson effects. In addition, at the extreme nodes, heat is also produced by the Peltier effect in the semiconductors and by the Joule effect in the electrical contacts. For simplicity, the following equations only show the expressions corresponding to the n semiconductors.

$$\dot{Q}_{n1} = N_{TEM} \cdot N_{tc} \cdot \left[\frac{-(\alpha_{p1} - \alpha_{n1})T_{n1}}{2} I + \frac{\rho_{u,n}^{sup}}{A_n} I^2 \right. \\ \left. + \rho_{n1} \cdot I^2 \frac{L_n/18}{A_n} - \sigma_{n1} \cdot I \frac{T_{n1} - T_{n2}}{2} \right] \tag{21}$$

$$\dot{Q}_{n(i)} = N_{TEM} \cdot N_{tc} \cdot \left(\rho_{n(i)} \cdot I^2 \frac{L_n/9}{A_n} \right. \\ \left. - \sigma_{n(i)} \cdot I \frac{T_{n(i-1)} - T_{n(i+1)}}{2} \right) \quad i = 2-9 \tag{22}$$

$$\dot{Q}_{n10} = N_{TEM} \cdot N_{tc} \cdot \left[\frac{-(\alpha_{p10} - \alpha_{n10})T_{n10}}{2} I + \frac{\rho_{u,n}^{sup}}{A_n} I^2 \right. \\ \left. + \rho_{n10} \cdot I^2 \frac{L_n/18}{A_n} - \sigma_{n10} \cdot I \frac{T_{n9} - T_{n10}}{2} \right] \tag{23}$$

In the calculation of the generated power, the Seebeck effect is considered. When an electrical resistance R_{Load} is connected to the system, the power generated in this case can be calculated according to Eq. (24), where N_{TEM} is the total number of thermoelectric modules installed, Et is the electromotive force generated per thermoelectric module (Eq. (25)), R_0 is the internal resistance of each module (Eq. (26)), and m is a parameter calculated with Eq. (27) in case the thermoelectric modules are connected in series, or with Eq. (28) in case of parallel connection.

$$P = N_{TEM} \cdot Et^2 \frac{m}{R_0 \cdot (m+1)^2} \tag{24}$$

As can be seen, the computational model contemplates both series and parallel electrical connection of the thermoelectric modules. In the specific case of the developed devices, the modules were connected in series in pairs.

$$Et = N_{tc} \cdot \left[\alpha_{p1}T_{p1} - \alpha_{n1}T_{n1} - \alpha_{p10}T_{p10} + \alpha_{n10}T_{n10} \right. \\ - \sigma_{p1}\frac{T_{p1} - T_{p2}}{2} + \sigma_{n1}\frac{T_{n1} - T_{n2}}{2} - \sigma_{p10}\frac{T_{p9} - T_{p10}}{2} \\ + \sigma_{n10}\frac{T_{n9} - T_{n10}}{2} - \sum_{i=2}^{9}\left(\sigma_{p(i)}\frac{T_{p(i-1)} - T_p(i+1)}{2} \right) \\ \left. + \sum_{i=2}^{9}\left(\sigma_{n(i)}\frac{T_{n(i-1)} - T_{n(i+1)}}{2} \right) \right] \tag{25}$$

$$R_0 = N_{tc} \cdot \left[\frac{L_p/9}{A_p}\left(\frac{\rho_{p1}}{2} + \frac{\rho_{p,n_p}}{2} + \sum_{i=2}^{n_p}\rho_{p(i)} \right) \right. \\ + 2\frac{\rho_{u,p}^{sup}}{A_p} + \frac{L_n/9}{A_n}\left(\frac{\rho_{n1}}{2} + \frac{\rho_{p,n_n}}{2} + \sum_{i=2}^{n_n}\rho_{n(i)} \right) \\ \left. + 2\frac{\rho_{u,n}^{sup}}{A_n} \right] \tag{26}$$

$$m^{ser} = \frac{R_{Load}}{N_{TEM} \cdot R_0} \tag{27}$$

$$m^{par} = \frac{N_{TEM} \cdot R_{Load}}{R_0} \tag{28}$$

3.1.3. Cold side heat exchangers

The cold side heat exchangers (CHE) also work by means of phase change thank to the heat pipes. As Fig. 6 shows, in the GTEGs developed by Catalán et al. [22] and Alegría et al. [23], each CHE consists of four copper heat pipes with water as working fluid, 8 mm diameter and 450 mm length inserted in a 70 mm x 70 mm plate base of aluminum in their boiling zone, and have aluminum fins of 0.5 mm thickness in their condensation zone to improve heat transmission by convection to the ambient.

In the electrical-thermal analogy, the thermal resistance corresponding to the CHE has been discretized by a single expression, since the phenomena involved in the operation of this type of heat exchanger are highly complex to simulate, and the experimental results of the field operation of these exchangers are available in [22] and [23]. Hence, this resistance (R_{CHE}) comes from analyzing the operation of the two thermoelectric generators already installed in the Timanfaya National Park, one of which is located in the medium temperature anomalies zone known as *Casa de los Camelleros* and the other in the high temperature zone, called *Islote Hilario*.
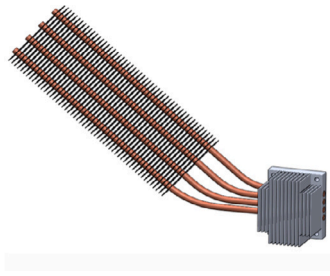
Fig. 6. Cold side heat exchanger based on phase change.

The instant operation data of each generator was used to calculate in each instant the thermal resistance of each device, according to Eq. (29), where T_C is the cold side temperature of the TEM, T_{amb} is the ambient temperature and $\dot{Q}_{CHE}$ is the heat flux through the cold side heat exchanger.

$$R_{CHE} = \frac{T_C - T_{amb}}{\dot{Q}_{CHE}} \tag{29}$$

The cold side heat flux, $\dot{Q}_{CHE}$, was calculated according to Eq. (30), where P_{TEM} is the power generated per TEM and η its efficiency, calculated according to the data sheet of the modules' manufacturer *Marlow* [34] considering the temperature difference between the hot and the cold side ($T_H - T_C$).

$$\dot{Q}_{CHE} = \frac{P_{TEM}}{\eta} \tag{30}$$

The thermal characterization of the CHE in the mentioned studies showed that the thermal resistance R_{CHE} is constant with the heat flux in the considered working values [12,23]. Additionally, R_{CHE} presents a decrease with the wind velocity, as the convection coefficients are improved with more intense winds. Figs. 7(a) and 7(b) represent the values introduced to the model as the cold side thermal resistances depending on the wind, in the medium temperature geothermal thermoelectric generator (MT-GTEG) and in the high temperature one (HT-GTEG), respectively.

Accordingly, the cold side thermal resistance used in the computational model follows Eq. (31) in the MT-GTEG and (32) in the HT-GTEG, introducing the wind velocity in km/h.

$$R^C = 0.3485 \cdot V^{-0.326} \tag{31}$$

$$R^C = 0.5154 \cdot V^{-0.329} \tag{32}$$

3.2. Experimental validation

To make this model a useful design tool, it is necessary to experimentally validate it. For this purpose, the power simulated by the model was represented (See Fig. 8) with respect to the real data of the power generated (daily average) between 2021 and 2022, using identical input parameters, which are shown in Table 1, considering 170 °C as the borehole temperature in MT and 465 °C in HT zones, according to [22,23]. The unknown input parameters of contact resistance between the heat exchangers and the thermoelectric modules both in the hot and cold sides (R_{co}^H and R_{co}^C) were adjusted, as well as the outcoming gas flow rate from the boreholes Q, as there is no current data of them [43]. These two parameters, whose values are shown in Table 2, were varied until obtaining a minimum deviation of the simulated output power with respect to the real power.

It can be seen in Fig. 8(a) that the model reliably reproduces the power generated in field by the developed MT-GTEG, presenting maximum deviations of $\pm10\%$, which is very satisfactory. Whereas the HT-GTEG, in view of the results in Fig. 8(b), an accurate fitting of the computational model developed has been achieved, since 98% of
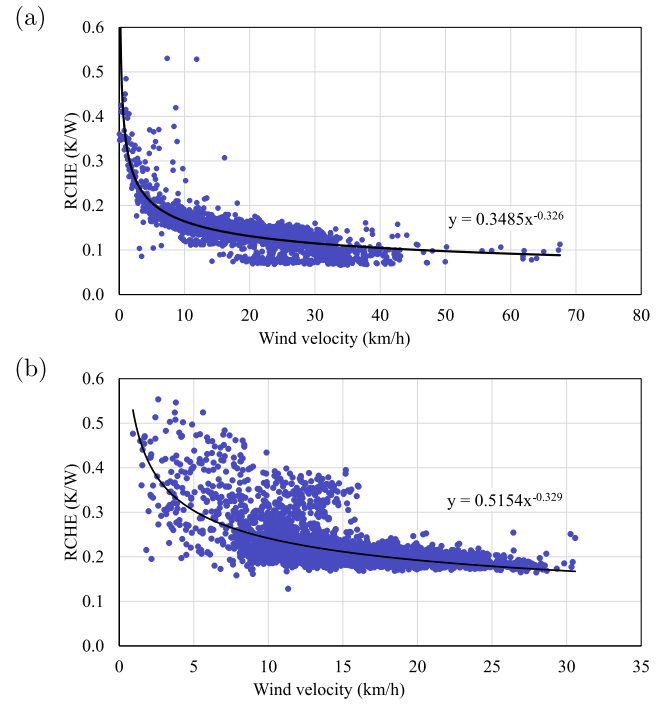

Fig. 7. Thermal resistance of the CHE vs. wind velocity. Average values each 1 min during 3 weeks. (a) MT-GTEG. (b) HT-GTEG.

Table 1
Known input parameters in the computational model.

Parameter	MT-GTEG	HT-GTEG
Borehole temperature (°C)	170	465
Borehole diameter (m)	0.15	0.305
TPCTs per borehole	1	1
TPCT diameter (m)	48	42.16
TPCT length (m)	2	2.5
TPCT thickness (m)	1.5	5
Water inside the TPCT (m)	0.375	0.50
Fins in the TPCT	31	0
Fins length (m)	17	0
Fins thickness (m)	2	0
Number of TEMs	6	8
Ambient temperature (°C)	instant	instant
Wind velocity (km/h)	instant	instant

Table 2
Adjusted input parameters in the computational model.

Parameter	MT-GTEG	HT-GTEG
Hot contact resist. (K/W)	0.025	0.02
Cold contact resist. (K/W)	0.025	0.02
Gas flow rate (m³/h)	1583	1590

the simulated points are very close to the diagonal, within $\pm10\%$ of the real generated power. The points with greatest distance to the diagonal correspond to days with wind speeds below 5 km/h, since, as shown in Fig. 7(b), there is a dispersion in the results of the cold side thermal resistance (R_{CHE}), when the wind speed is low, because the computational model does not take into account thermal inertia or radiation. The vast majority of the points correspond to days with wind speeds over 5 km/h, which are very close to the diagonal, within $\pm5\%$ of the real values. At high wind speeds, the ambient conditions around the cold side heat exchangers are homogeneous, however, the heterogeneities in these conditions when there is little wind and ground heat can reach the cold heat exchangers are considered only in the characterization of the thermal resistance of the CHE depending on the
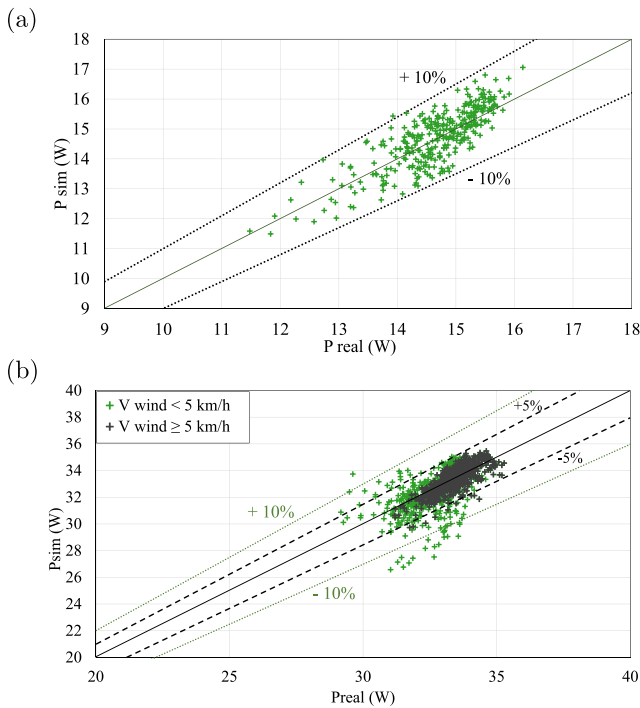
(a)

(b)

Fig. 8. Simulated power within ±10% of the real power generated. (a) by the MT-GTEG (thermosyphon with 6 TEMs). (b) by the HT-GTEG (8 TEMs).
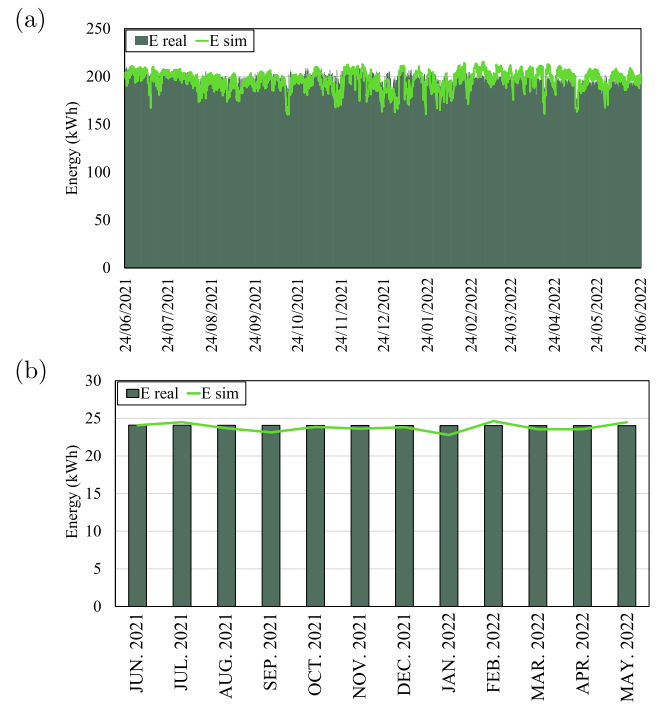
(a)

(b)

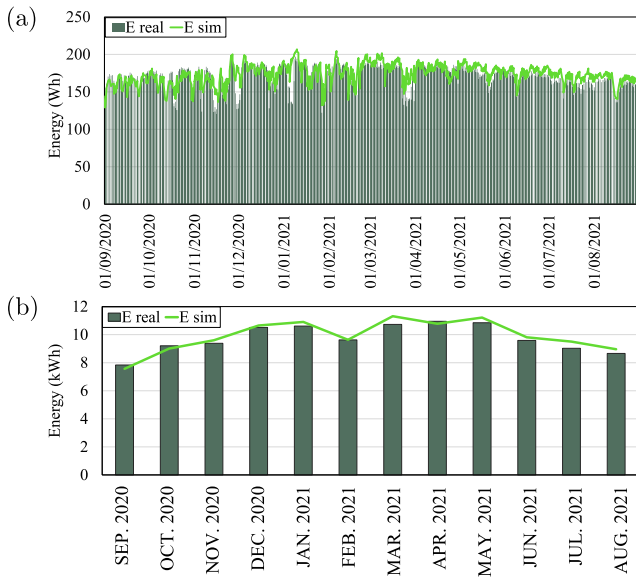**Fig. 9.** Simulated and real energy generated by the MT-GTEG (thermosyphon with 6 TEMs). (a) per day over one year. (b) per month over one year.

(a)

(b)

Fig. 10. Simulated and real energy generated by the HT-GTEG (8 TEMs). (a) per day over one year. (b) per month over one year.

of the deflector mentioned in Section 2, this model reliably reproduces the energy generated during the majority of the time, accurately representing peaks and valleys of energy. Thus, in Fig. 9(b) it can be seen that the model is completely reliable and that the slight variations that occur due to wind direction do not significantly affect the monthly prediction. The value of the energy generated by the GTEG throughout the year was 117.17 kWh, while that simulated by the model is 119.12 kWh, achieving an error of 1.6%.

As in the medium temperature GTEG, the simulation of the energy generated during one year for the high temperature GTEG reproduces both peaks and valleys of generation, as can be observed in Fig. 10(a). Once again, the slight variations do not influence the model's ability to predict the energy generated throughout each month, as Fig. 10(b) shows. Thus, this model also reproduces in a totally reliable way the electrical energy that can be generated per month and throughout a whole year by the thermoelectric generator for high temperature geothermal energy, since the value of total energy generated during this year was 287.13 kWh, and the simulated value, 285.69 kWh, which means an error of 0.5%.

However, while the most important aspect of this model is its ability to predict the power that these devices can generate under different conditions, it is also important to determine the model's capability to reproduce the temperatures on the hot and cold sides of the modules. For this reason, the experimental temperature values of the modules' hot and cold sides have been obtained, and have been plotted together with the simulated values, the temperatures of the hot (borehole) and cold (ambient) reservoirs, as well as the experimental and simulated power and the wind during a two-day period with a wide variation in wind velocity, as seen in Fig. 11.

Thanks to the thermosyphon effect, the condensation temperature in the area where the modules are installed is constant (equal to the saturation temperature corresponding to the pressure inside), so the temperatures of the hot sides of the different modules are the same.

It can be seen in Fig. 11 that the power performance is very accurate, even managing to represent specific generation peaks such as the one occurring on 2-10-2020 between 12:00 and 12:30, which

wind (Fig. 7(b)). This makes the data under low-wind conditions more scattered, and less disperse when the wind velocity is high.

Since the electrical generation is, ultimately, the most important in terms of what the computational model should predict, the real energy generated by each on the GTEGs during one whole year has been represented and compared to the energy simulated by the model.

For the thermosyphon with 6 modules of the MT-GTEG, the daily values are shown in Fig. 9(a). It can be observed that, although some days the real energy generated is lower than that simulated by the model, corresponding to days with S-SW wind carrying the hot gases from the borehole to the cold side exchangers due to the configuration
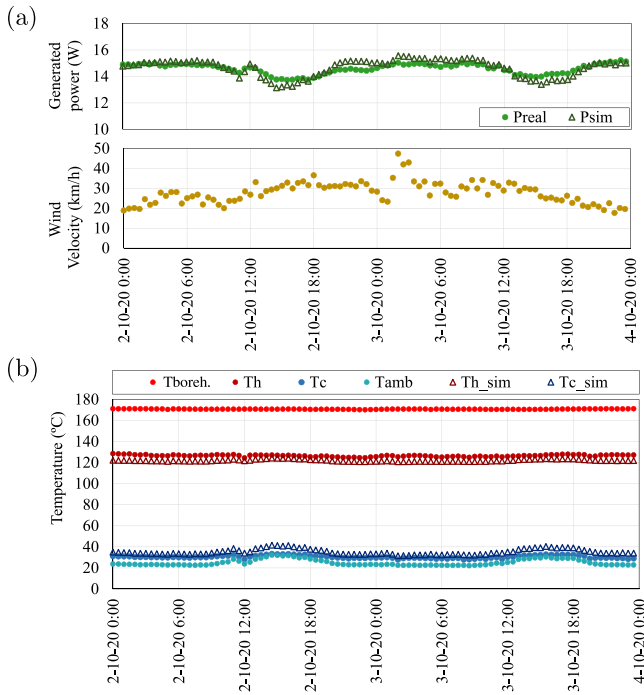
Fig. 11. (a) Simulated and real power generated by the MT-GTEG (thermosyphon with 6 TEMs) and wind velocity. (b) Simulated and real temperatures of the hot and cold side of the TEMs, and temperature of the borehole and the ambient.
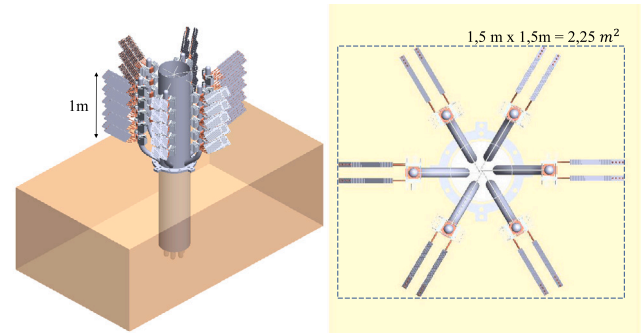

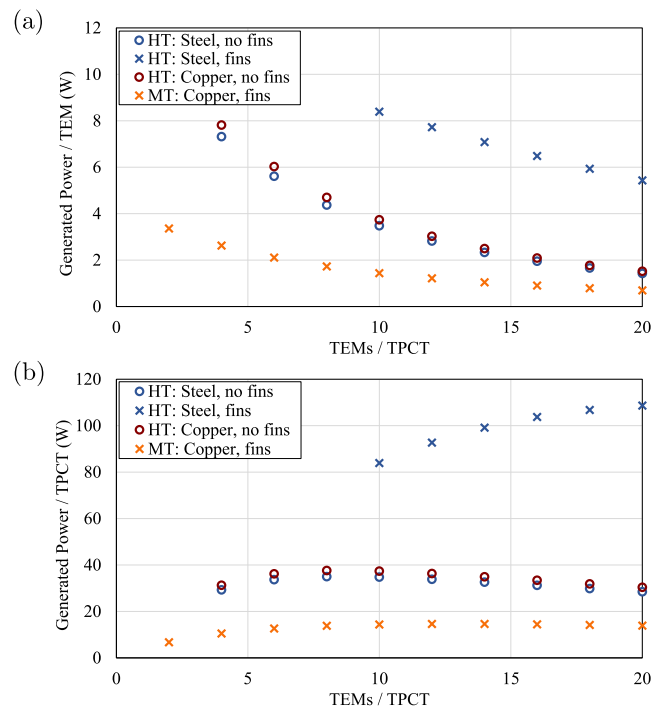Fig. 12. Proposed GTEG for a high-scale installation.

Fig. 13. Computational study of the influence of the number of thermoelectric modules installed per TPCT with different TPCT configurations. (a) Power generated per TEM. (b) Power generated per TPCT.

was caused by a decrease in the ambient temperature and an increase in the wind speed. The temperature setting is also very reliable, with simulated temperatures on the hot and cold side very close to the real ones, presenting differences of less than 10%.

This way, it is validated that this model is able to correctly reproduce the behaviour of each part of the generator: hot-side exchanger, thermoelectric modules and cold-side exchangers.

4. Study of the energy potential in Lanzarote

The final objective is to take advantage of the geothermal anomalies of the Timanfaya National Park to produce electrical energy in a renewable and less invasive way. Therefore, although further studies are required in order to deeper know the geothermal potential of the island, it is important to estimate the electrical energy that could be generated if harnessing the known geothermal anomalies by means of a larger-scale installation.

Regarding a higher-scale installation, it is very important to make use of all the available space in a borehole. In a standard borehole of 300 mm diameter there is room for 6 thermosyphons, and the deflector must direct the hot gases to the upper part in order not to interfere with the cold side heat exchangers. That is why the proposed design corresponds to the one shown in Fig. 12: 6 thermosyphons per borehole with a central chimney-type deflector, occupying an area of $2.25 \, \text{m}^2$. Hence, to determine in detail the number of thermoelectric modules that each TPCT should contain, as well as the configuration of the thermosyphons appropriate for each temperature level of geothermal anomalies, the developed computational model has been employed, taking into account the material (copper or steel) and the use of fins.

Different configurations have been simulated to obtain the generated power with respect to the number of thermoelectric modules installed. In the case of MT anomalies, the use of a copper finned TPCT is clear, so as to improve heat transmission. But in HT anomalies, the analysed options are copper/steel TPCT, with/without fins. The boundary conditions are the ones presented in Tables 1 and 2 including

the average values of ambient temperature and wind in Lanzarote (22.1 °C and 21.2 km/h [44]).

Fig. 13 shows the results, from which the copper finned option in HT anomalies has been removed due to the high temperatures reached in the modules' sides. Values with modules' sides temperatures higher than the maximum allowed according to the manufacturer [34] have also been removed. In Fig. 13(a), the decrease in the power generated per thermoelectric module as the number of thermoelectric modules per thermosypon increases can be observed, which is completely consistent with the results previously obtained computationally by Catalán et al. [32] and experimentally by Alegría et al. [12,23].

In view of the results, for a high-scale installation, to achieve a compromise between constructive simplicity, visual impact and power output near the optimum, the design for medium temperature anomalies consists of a GTEG with 10 TEMs and a copper finned TPCT, and for high temperature anomalies consists of a GTEG also with 10 TEMs but with a steel finned TPCT.

Finally, considering the mentioned characteristics for each kind of anomalies and taking into account the available area in zones with

Table 3

Estimation of the annual electrical energy that could be generated by a large-scale installation occupying the zones with medium and high temperature geothermal anomalies.

Type of geothermal anomaly	MT	HT
P/TEM (W)	1.43	8.39
P/Borehole (W)	86.28	503.46
P/Occupied area (W/m^2)	38.35	223.76
E_{YEAR}/Occupied area (MWh/m^2)	0.34	1.96
Area of anomalies (m^2)	4000	3000
E_{YEAR} (GWh)	1.36	5.88
E_{YEAR} total (GWh)		7.24

medium temperature and with high temperature geothermal anomalies, Table 3 shows the electrical energy that could be generated in Lanzarote with GTEGs as the designed in Fig. 12, composed by 10 thermoelectric modules in each thermosyphon and 6 thermosyphons in each borehole, occupying $2.25\,m^2$ per GTEG.

The energy per unit area generated by the installation considered is 1.03 MWh/m^2, since geothermal energy is present 24 h a day, 365 days a year. If this result is compared with the energy that could be generated nowadays by a photovoltaic installation of 200 Wp/m^2 occupying the same surface, in Lanzarote, by means of a grid connected system with crystalline silicon panels, with optimum inclination and azimuth and standard losses of 14%, this installation produces an annual energy of 0.36 MWh/m^2 [45]. This means 2.9 times more with GTEGs than with PV panels, given that photovoltaic is weather-dependent, while geothermal is totally continuous and stable. Taking into account that the average consumption of a household in Spain is 3487 kWh per year [46], the area required by GTEGs to generate the energy consumed by a household annually is $3.38\,m^2$. It should be noted that the objective is not to cover the entire surface of geothermal anomalies of the Timanfaya National Park with GTEGs, since this would lose the natural value of this environment, but it is intended to give an approximation of the existing potential to generate electricity in a renewable way and taking advantage of a genuine resource. In addition, there are more anomalies outside the park, around the central and southern eruptive fissures [47], so further studies are needed to determine the exact area with anomalies and the temperatures reached. The use of these temperatures outside the park through GTEGs would have a more direct application, since there are nearby houses that could benefit from this geothermal source for self-consumption.

5. Conclusions

In this work a computational model has been developed by employing the finite difference method. This model represents, by means of the thermal-electrical analogy, all the phenomena that occur in a geothermal thermoelectric generator whose heat exchangers operation is based on phase change, from the heat exchanger on the hot side that is inserted in a geothermal borehole, through the thermoelectric modules, to the heat exchanger on the cold side that releases its heat to the environment. This is a versatile tool that permits varying the configuration of the thermoelectric generator considered, as well as the boundary conditions of the zone where they are installed. After the data analysis of the only geothermal thermoelectric generators installed and operating in field worldwide, the real values of the generated power were compared with the power simulated by the model, obtaining a very good accuracy, with relative errors lower than ±10%. Furthermore, this model is capable of reliably and accurately predicting the annual energy generated both in medium and high temperature geothermal anomalies, with a relative error of 1.6% and 0.5%, respectively. Therefore, it represents a novel and very useful tool when designing thermoelectric generators for geothermal energy and adapting them to the conditions of each environment where they need to be installed. This tool will reduce time and costs in experimentation,

given that these geothermal thermoelectric generators are completely innovative.

To demonstrate the usefulness of the developed model, it has been used to determine the most appropriate installation depending on the temperature conditions. The most appropriate installation consists, in MT anomalies, of GTEGs with finned copper thermosyphons, while in HT zones, it consists in finned steel thermosyphons.

Then, a calculation has been made of the energy that could be generated annually by a high-scale installation of geothermal thermoelectric generators in Lanzarote, taking advantage of the geothermal anomalies area characterized so far. The annual energy that could be generated is of 7.24 GWh, which, translated into energy per unit of occupied area, means 1.03 MWh/m^2, 2.9 times the energy that could be generated with a photovoltaic panel given the continuity of geothermal energy and its independence of the weather.

This not only demonstrates the potential of harnessing this hitherto untapped energy source by means of this novel system of low environmental impact, but also shows the usefulness of the developed computational model for the design of an installation, since it has made possible to determine the most suitable configuration of thermoelectric generators, as well as to calculate the potential of energy generation with very promising results.

Declaration of competing interest

The authors declare that they have no known competing financial interests or personal relationships that could have appeared to influence the work reported in this paper.

Data availability

The data that has been used is confidential.

References

[1] R.E. de España, El sistema eléctrico español: Avance 2021, 2021, URL https://www.ree.es/es/glosario.

[2] Renewables now. Renewables 2020. Global status report, REN 21 (2021).

[3] E. Comission, European green deal. 2050 long-term strategy, Clim. Action (2020) URL https://ec.europa.eu/clima/eu-action/climate-strategies-targets/2050-long-term-strategy_en.

[4] G. of the Canary Islands, MITECO, IDAE, Sustainable energy strategy in the canary islands, 2022.

[5] P. Armenti, L. Marinoni, G. Pasquare, Geological map of the island of lanzarote, ESF Meet. Canarian Volcanism, Lanzarote (1989) 198–200.

[6] R. Ortiz, V. Araña, C. Valverde, Aproximacion al conocimiento del mecanismo de la erupcion de 1730-1736 en lanzarote, Proyecto Investigación n 449 CSIC-CAICYT 449 (1986).

[7] J.L. Díez, J. Yuguero, R. Ortiz, V. Araña, Termometrias y modelos matemáticos para el estudio de gradientes térmicos superficiales en lanzarote (islas canarias), Proyecto Investigación n 449 CSIC-CAICYT 449 (1986).

[8] V.R. Troll, J.C. Carracedo, The geology of lanzarote, Geol. Canary Islands (2016) 483–530, http://dx.doi.org/10.1016/b978-0-12-809663-5.00007-4.

[9] V. Araña, R. Ortiz, J. Yuguero, Thermal anomalies in lanzarote (canary islands), 2, 1973.

[10] E. Martinez, J. Prieto, A. Centellas, Guia del Parque Nacional de Timanfaya, O.A. Parques Nacionales, 2005.

[11] J.L. Diez, J.F. Albert, F. Torres, A. Valentin, Shallow HDR geothermal field in lanzarote (canary islands). Potential evaluation and heat extraction tests. Proyecto joule., 1991, URL https://cordis.europa.eu/project/id/JOUG0004/es.

[12] P. Alegria, L. Catalan, M. Araiz, A. Rodriguez, D. Astrain, Experimental development of a novel thermoelectric generator without moving parts to harness shallow hot dry rock fields, Appl. Therm. Eng. 200 (2022) http://dx.doi.org/10.1016/j.applthermaleng.2021.117619.

[13] D. Rowe, in: D. Rowe (Ed.), Thermoelectrics Handbook, CRC Press, 2006, http://dx.doi.org/10.1201/9781420038903.

[14] D. Astrain, J.G. Vian, A. Martinez, A. Rodriguez, Study of the influence of heat exchangers' thermal resistances on a thermoelectric generation system, Energy 35 (2010) 602–610, http://dx.doi.org/10.1016/j.energy.2009.10.031.

[15] C. Liu, P. Chen, K. Li, A 500 W low-temperature thermoelectric generator: Design and experimental study, Int. J. Hydrogen Energy 39 (2014) 15497–15505, http://dx.doi.org/10.1016/j.ijhydene.2014.07.163.

[16] C. Liu, P. Chen, K. Li, A 1 KW thermoelectric generator for low-temperature geothermal resources.

[17] C. Suter, Z.R. Jovanovic, A. Steinfeld, A 1kwe thermoelectric stack for geothermal power generation - modeling and geometrical optimization, Appl. Energy 99 (2012) 379–385, http://dx.doi.org/10.1016/j.apenergy.2012.05.033.

[18] R. Ahiska, H. Mamur, Design and implementation of a new portable thermoelectric generator for low geothermal temperatures, IET Renew. Power Gener. 7 (2013) 700–706, http://dx.doi.org/10.1049/iet-rpg.2012.0320.

[19] R. Dell, C.S. Wei, M.T. Petralia, G. Gislason, R. Unnthorsson, Thermoelectric powered security systems in iceland using a geothermal steam pipe as a heat source, Proceedings 2 (2018) 440, http://dx.doi.org/10.3390/icem18-05309.

[20] Y. Zhao, Y. Fan, W. Li, Y. Li, M. Ge, L. Xie, Experimental investigation of heat pipe thermoelectric generator, Energy Convers. Manage. 252 (2022) 115123, http://dx.doi.org/10.1016/j.enconman.2021.115123, URL https://linkinghub.elsevier.com/retrieve/pii/S0196890421012991.

[21] L. Catalan, P. Aranguren, M. Araiz, G. Perez, D. Astrain, New opportunities for electricity generation in shallow hot dry rock fields: A study of thermoelectric generators with different heat exchangers, Energy Convers. Manage. 200 (2019) http://dx.doi.org/10.1016/j.enconman.2019.112061.

[22] L. Catalan, P. Alegria, A. Araiz, D. Astrain, Field test of a geothermal thermoelectric generator without moving parts on the hot dry rock field of Timanfaya National Park, Appl. Therm. Eng. 222 (2023) 119843, http://dx.doi.org/10.1016/j.applthermaleng.2022.119843.

[23] P. Alegria, L. Catalan, M. Araiz, A. Casi, D. Astrain, Thermoelectric generator for high temperature geothermal anomalies: Experimental development and field operation, Geothermics 110 (2023) http://dx.doi.org/10.1016/j.geothermics.2023.102677, Cited by: 0; All Open Access, Hybrid Gold Open Access.

[24] A. Ioffe, Semiconductor Thermoelements and Thermoelectric Cooling, Infosearch Limited, London, 1957.

[25] J. Stockholm, D. Stockholm, Thermoelectric modelling of a cooling module with heat exchangers, in: Proceedings of the XI International Conference on Thermoelectrics, 1992.

[26] D. Kondratiev, L. Yershova, TE coolers computer simulation: incremental upgrading of rate equations approach, in: Proceedings of the VI European Workshop on Thermoelectrics, 2001.

[27] D. Astrain, J.G. Vián, J. Albizua, Computational model for refrigerators based on peltier effect application, Appl. Therm. Eng. 25 (2005) 3149–3162, http://dx.doi.org/10.1016/j.applthermaleng.2005.04.003.

[28] A.M. Echeverri, Estudio y desarrollo de sistemas termoeléctricos para el aprovechamiento del calor residual en la generación de energía eléctrica, Universidad Pública de Navarra, Pamplona, 2012.

[29] A. Martinez, D. Astrain, A. Rodriguez, Dynamic model for simulation of thermoelectric self cooling applications, Energy 55 (2013) 1114–1126, http://dx.doi.org/10.1016/j.energy.2013.03.093.

[30] P.A. Garacochea, Estudio y optimización de los sistemas de intercambio de calor en generación termoeléctrica aplicada al aprovechamiento del calor residual, Universidad Pública de Navarra, Pamplona, 2015.

[31] M. Araiz, L. Catalan, O. Herrero, G. Perez, A. Rodriguez, The importance of the assembly in thermoelectric generators, Bringing Thermoelectr. Reality (2018) http://dx.doi.org/10.5772/intechopen.75697.

[32] L. Catalan, M. Araiz, P. Aranguren, D. Astrain, Computational study of geothermal thermoelectric generators with phase change heat exchangers, Energy Convers. Manage. 221 (2020) http://dx.doi.org/10.1016/j.enconman.2020.113120.

[33] L. Catalan, Design and Experimental Development of Thermoelectric Generators for Shallow Geothermal Anomalies of Volcanic Origin, Universidad Pública de Navarra, Pamplona, 2020.

[34] Marlow Industries Inc., Marlow TG12-8 Datasheet, 2022, pp. 1–2, URL http://www.marlow.com/media/marlow/product/downloads/tg12-8-01ls/TG12-8_Data_Sheet_RevM.pdf.

[35] P.B. Zhou, Finite Difference Method, Springer Berlin Heidelberg, Berlin, Heidelberg, 1993, pp. 63–94, http://dx.doi.org/10.1007/978-3-642-50319-1_3.

[36] H. Forster, N. Zuber, Dynamics of Vapour Bubbles and Boiling Heat Transfer, Am. Inst. Chem. Eng. J. 1 (1955) 531–535.

[37] W. Rohsenow, J. Hartnett, Y. Cho, Handbook of Heat Transfer, 3rd edition, McGraw-Hill Handbooks, 1998.

[38] A.J. Chapman, Fundamentals of Heat Transfer, Macmillan Publishing Company, New York, 1987.

[39] F.P. Incropera, D.P. Witt, Fundamentals of Heat Transfer, fourth ed., Prentice Hall.

[40] S. Lee, S. Song, V. Au, K.P. Moran, Constriction/spreading resistance model for electronics packaging, in: Proceedings of the 4th ASME/JSME Thermal Engineering Conference, Vol. 4, 1995, pp. 199–206.

[41] A. Rodríguez, J.G. Vián, D. Astrain, A. Martínez, Computational model and test bench for thermoelectric power generation, for thermoelectric parameters dependent on the temperature, in: International Conference on Thermoelectrics, ICT, Proceedings, 2006, pp. 300–304, http://dx.doi.org/10.1109/ICT.2006.331374.

[42] P. Aranguren, D. Astrain, A. Rodriguez, A. Martinez, Experimental investigation of the applicability of a thermoelectric generator to recover waste heat from a combustion chamber, Appl. Energy 152 (2015) 121–130, http://dx.doi.org/10.1016/j.apenergy.2015.04.077.

[43] I.G.M. Español, Evaluación del potencial geotérmico superficial de Montañas de Fuego como Sistema de Roca Caliente Seca, Tech. rep., 1992.

[44] Meteoblue, Clima lanzarote, 2022, URL https://www.meteoblue.com/es/tiempo/historyclimate/climatemodelled/lanzarote_espa%C3%B1a_2515699.

[45] European Comission, Photovoltaic geographical information system, 2022, URL https://re.jrc.ec.europa.eu/pvg_tools/en/.

[46] Instituto para la Diversificación y Ahorro de la Energía and Eurostat, Consumos del sector residencial en españa, 2022, URL https://www.idae.es/informacion-y-publicaciones/estudios-informes-y-estadisticas.

[47] ITER, INVOLCAN, AIET, UPNA, IGME, Final report of project electrovolcan. Reference RTC-2017-6628-3, financed with FEDER funds, 2021, URL https://www.iter.es/portfolio-items/electrovolcan/.